

Two polymorphs of a new intermetallic Ce₂Rh₂Ga – crystal structure and physical properties

Sergey Nesterenko¹, Anna Tursina¹, Mathieu Pasturel², Sindisiwe Xhakaza³, André Strydom^{3,4}

¹ *Department of Chemistry, Lomonosov Moscow State University, 119991 Moscow, Russia*

² *Univ Rennes, CNRS, ISCR – UMR6226, F-35000 Rennes, France*

³ *Highly Correlated Matter Research Group, Physics Department, University of Johannesburg,
PO Box 524, Auckland Park 2006, South Africa*

⁴ *Max Planck Institute for Chemical Physics of Solids, 40 Nöthnitzerstr., D-01187 Dresden,
Germany*

Highlights

- Ce₂Rh₂Ga crystallizes in Pr₂Co₂Al-type (LT) and La₂Ni₃-type (HT) structures.
- The transition occurs at 864(5)°C
- Both structures can be described by different stacking of Ce-centered CeGa₄ building blocks.
- HT-Ce₂Rh₂Ga exhibits a phase transition, putatively of magnetic nature, at the unusually high temperature of 128.5 K

Keywords: cerium intermetallics; gallides; crystal structure; magnetic properties

Abstract

We report on the synthesis and physical properties of the new ternary intermetallic Ce₂Rh₂Ga. Its formation and dimorphism have been investigated by powder and single crystal X-ray diffractometry, as well as by differential thermal analyses. LT- and HT-Ce₂Rh₂Ga can be obtained by the chosen respective thermal treatment. The high-temperature form (HT-Ce₂Rh₂Ga), stable above 864(5)°C, is orthorhombic La₂Ni₃-type [*Cmce*, *oS20*, *a*=5.851(2) Å, *b*=9.618 (2) Å, *c*=7.487 (2) Å, *V*=421.3(2) Å³]; the low-temperature form (LT-Ce₂Rh₂Ga), stable below this temperature, is monoclinic Pr₂Co₂Al- (Ca₂Ir₂Si-) type [*C2/c*, *mS20*, *a*=10.0903(6) Å, *b*=5.6041(3) Å, *c*=7.8153(4) Å, *β*=104.995(3)°, *V*=426.88(4) Å³]. The magnetic measurements were conducted on two different samples, namely on the LT-Ce₂Rh₂Ga and the other on the HT-Ce₂Rh₂Ga sample. The HT-Ce₂Rh₂Ga compound is found to exhibit a phase transition at 128.5 K. By virtue of the sharp peak anomaly in the temperature dependence of the magnetic susceptibility this phase transition is plausibly of antiferromagnetic origin, but occurs at a remarkably high temperature compared to what is typical for Ce binary and ternary compounds. LT- Ce₂Rh₂Ga has a ground

state of ferromagnetic nature which sets in at a paramagnetic-to-ferromagnetic phase transition at 5.2 K.

1. Introduction

The R_2T_2X series of compounds (with R = rare earth, T = transition metal and $X = p$ -metal), the so-called 2:2:1 family, are known to exhibit a wide variety of physical properties at low temperature. Their crystallographic characteristics and magnetic data have been summarized in review articles (see *e.g.* [1-3]). In particular, in the ternary systems with $X = \text{In}$, the known R_2T_2X phases show ground states ranging from magnetically ordered Kondo compounds for $T = \text{Pd, Cu, and Ag}$ via a heavy fermion behavior in $\text{Ce}_2\text{Pt}_2\text{In}$ to intermediate valence for $T = \text{Ni and Rh}$ [4]. The $\text{Ce}_2\text{Ni}_2\text{Sn}$ stannide behaves like a Kondo system and orders antiferromagnetic below $T_N = 4.7$ K [5]. The cerium-based intermetallics $\text{Ce}_2\text{Ni}_{1.88}\text{Cd}$ [6, 7] as well as $\text{Ce}_2\text{Ni}_2\text{Ga}$ [8] exhibit a fluctuating valence. $\text{Yb}_2\text{Ni}_2\text{Al}$ and $\text{Yb}_2\text{Pd}_2\text{Sn}$ were reported as heavy fermion systems with magnetically non-ordered ground states [9, 10].

Most of R_2T_2X phases crystallize in the four structure types: $\text{Mo}_2\text{B}_2\text{Fe}$ (tetragonal, $P4/mbm$) [11], $\text{Er}_2\text{Au}_2\text{Sn}$ or $\text{U}_2\text{Pt}_2\text{Sn}$ (tetragonal, $P4_2/mnm$) - a superstructure of $\text{Mo}_2\text{B}_2\text{Fe}$ [12, 13], $\text{W}_2\text{B}_2\text{Co}$ (orthorhombic, $Immm$) [14], and $\text{Mn}_2\text{B}_2\text{Al}$ (orthorhombic, $Cmmm$) [15].

Five less common types are encountered in literature. Two of these are monoclinic ones: $\text{HT-Pr}_2\text{Co}_2\text{Al}$ or $\text{Ca}_2\text{Ir}_2\text{Si}$ ($C2/c$) - stacking variant of the $\text{W}_2\text{B}_2\text{Co}$ [16, 17] - and $\text{LT-Nd}_2\text{Cu}_2\text{Cd}$ ($C2/c$, own structure type) - superstructure of $\text{Mn}_2\text{B}_2\text{Al}$ [18]; the other three structures are orthorhombic: La_2Ni_3 ($Cmce$) [19], $o\text{-La}_2\text{Ni}_2\text{In}$ ($Pbam$) [20], and $\text{Ca}_2\text{Pd}_2\text{Ge}$ ($Fdd2$) [21]. Only a few representatives of these types are reported to date [22-26].

The structural diversity of the R_2T_2X family is frequently accompanied by polymorphic phenomena between these structure types. A structural transformation from $\text{Mo}_2\text{B}_2\text{Fe}$ to $\text{W}_2\text{B}_2\text{Co}$ -type was observed in the $\text{R}_2\text{Ni}_2\text{Sn}$ ($R = \text{Ce, Pr, Nd, Sm, Gd - Tm, Lu}$) system as a function of the rare-earth size or external pressure [27, 28]. Also, depending on the size of the rare earth element, several groups of indides and stannides crystallize with the $\text{Mo}_2\text{B}_2\text{Fe}$ -type or the $\text{Er}_2\text{Au}_2\text{Sn}$ structure [29, 30]. A transition from the $\text{Mo}_2\text{B}_2\text{Fe}$ -type to the $\text{Mn}_2\text{B}_2\text{Al}$ -type, provided by geometrical reasons or temperature, was found in the $\text{RE}_2\text{Ni}_2\text{X}$ ($X = \text{In or Cd}$) series. The latter transition is of a reconstructive nature [31, 32].

Polycrystalline Mo_2FeB_2 -type $\text{U}_2\text{Pt}_2\text{In}$ transforms via a displacive phase transition to the $\text{Er}_2\text{Au}_2\text{Sn}$ -type in the process of single crystal growth [33]. $\text{Pr}_2\text{Co}_2\text{Al}$ is dimorphic with a $\text{W}_2\text{B}_2\text{Co}$ -type low-temperature modification and a monoclinic (space-group $C2/c$) high-temperature modification [16]. According to [20], $\text{La}_2\text{Ni}_2\text{In}$ crystallizes with the orthorhombic

(*Pbam*) or tetragonal $\text{Mo}_2\text{B}_2\text{Fe}$ (*P4/mbm*) modification depending on annealing temperature. Interestingly, the same transformation takes place in the course of the hydrogenation of $\text{La}_2\text{Ni}_2\text{In}$, during which the symmetry changes from tetragonal to orthorhombic [34]. Finally, in the Gd-Co-Ga system, the compound with the $\text{W}_2\text{B}_2\text{Co}$ -type structure is formed at the stoichiometric composition, but the Ga-deficient compound with $\text{Gd}_2\text{Co}_{2.9}\text{Ga}_{0.1}$ composition crystallizes in the $\text{Mn}_2\text{B}_2\text{Al}$ -type structure [35, 36], and in the Dy-Ni-Si system the variation of alloy composition from $\text{Dy}_2\text{Ni}_{2.35}\text{Si}_{0.65}$ to $\text{Dy}_2\text{Ni}_{2.5}\text{Si}_{0.5}$ leads to crystallization of $\text{W}_2\text{B}_2\text{Co}$ - or La_2Ni_3 -type compounds [36].

In the course of our investigations on the ternary Ce-Rh-Ga system, we have discovered a new compound, namely $\text{Ce}_2\text{Rh}_2\text{Ga}$. As it turned out, it is dimorphic, with the high temperature form adopting the orthorhombic La_2Ni_3 -type structure and the low temperature form crystallizing in the monoclinic $\text{Pr}_2\text{Co}_2\text{Al}$ -type, and shows a new type of phase transition in the $\text{R}_2\text{T}_2\text{X}$ family. Synthesis, crystal structures determination and LT physical properties for $\text{Ce}_2\text{Rh}_2\text{Ga}$ polymorphs and $\text{La}_2\text{Rh}_2\text{Ga}$ are reported herein. Preliminary data were presented at the SCTE 2018 conference [37].

2. Experimental

The alloys were prepared by arc-melting (Arc Melter AM/0.5, Edmund Bühler GmbH) appropriate amounts ((Ce or La) $40\text{Rh}40\text{Ga}20$ (at.%) of the constituent elements under a high-purity argon atmosphere in a water-cooled copper hearth. The purities of the starting materials were 99.85 % for Ce and La, 99.95 % for Rh, and 99.999 % for Ga. The ingots were remelted three times to ensure homogeneity. Then both the resulting cerium and lanthanum ingots were divided into two parts. First halves of Ce based and La based samples were annealed at 700 and the second ones at 900°C for 30 days in evacuated quartz tubes and then quenched in cold water.

Both the composition and the homogeneity of the annealed samples were checked by microprobe analysis using a Carl Zeiss LEO EVO 50XVP scanning electron microscope equipped with an INCA Energy 450 (Oxford Instruments) EDX-spectrometer.

X-ray powder diffraction was performed at room temperature with the use of a STOE STADI-P transmission diffractometer with $\text{CuK}\alpha_1$ radiation ($\lambda = 1.54056 \text{ \AA}$) in the $10 - 90^\circ$ 2θ range with a step size of 0.01° .

Single crystals of HT- $\text{Ce}_2\text{Rh}_2\text{Ga}$ and $\text{La}_2\text{Rh}_2\text{Ga}$ were separated from the respective as-cast samples, whereas single crystal of LT- $\text{Ce}_2\text{Rh}_2\text{Ga}$ was found in the annealed at 700°C sample. Single crystal X-ray diffraction data were collected at room temperature either on a Bruker Apex II (Mo $K\alpha$ radiation) or on a CAD4 Enraf Nonius (Ag $K\alpha$ radiation) diffractometers. The crystal

structures were refined by the full-matrix least-squares method in the anisotropic approximation for all atoms using either the SHELXL-97 software [38] or SHELXL-2015/1 one. Further details of the crystal structure investigations are listed in Table 1 and may be obtained from the Fachinformationszentrum Karlsruhe, 76344 Eggenstein-Leopoldshafen, Germany (Fax: +49-7247-808-666; E-Mail: crysdata@fiz-karlsruhe.de, http://www.fiz-karlsruhe.de/request_for_deposited_data.html) on quoting the depository numbers CSD 434348 (LT-Ce₂Rh₂Ga) and CSD 434386 (HT-Ce₂Rh₂Ga). The crystal structure of La₂Rh₂Ga was deposited to the joint CCDC/FIZ Karlsruhe database via www.ccdc.cam.ac.uk with the reference number 1941455. Final atomic coordinates and equivalent isotropic displacement parameters are listed in Table 2, and the most important bond distances for Ce₂Rh₂Ga polymorphs are given in Table 3.

The annealed samples of Ce₂Rh₂Ga were analyzed by differential thermal analysis (DTA) using a NETZSCH Leading Thermal Analysis STA 449 F1 Jupiter Platinum RT apparatus. The polycrystalline samples (~30 mg) were put in a small Al₂O₃ crucible, and the subsequent measurement was conducted under a continuous He flow of 30 mL min⁻¹. The cooling and heating rates were 20 °C min⁻¹. An empty Al₂O₃ crucible was used as a reference.

The magnetic susceptibility and heat capacity were measured as function of temperature in high resolution using a Dynacool Physical Properties Measurement System from *Quantum Design* (San Diego, USA). In the case of magnetic susceptibility, data were recorded in both warming and cooling modes in order to investigate the reversibility of the phase transition.

3. Results

3.1 Phase analysis

Microprobe analysis on both annealed Ce₂Rh₂Ga samples confirmed the chemical composition and homogeneous distribution of the elements with negligible amount of CeRhGa phase [39]. As this equiatomic ternary phase shows intermediate valent behavior without magnetic ordering [40, 41] we expect its presence in our magnetic study on Ce₂Rh₂Ga to be of no consequence.

The X-ray powder patterns of these samples were different depending on the thermal treatment used, and at the same time the crystal structure of the sample annealed at 900°C does not differ from the as-cast ones. DTA was used to establish the reason for this difference (Fig. 1, and Fig. S1 in Supplementary). When heating of the sample annealed at 700°C, one relatively weak endothermic peak was detected at 864(5)°C, that may be attributed to the low temperature (LT) – high temperature (HT) polymorphous transformation, followed by melting at 970(5)°C. It is worth noticing that the reversible polymorphic reaction is not detected in the cooling branch of

DTA scan; this could be due to the small amount of heat and slow kinetics associated to this reaction.

The XRD data refinement of polycrystalline samples reveals that the sample annealed at 700°C consisted solely of the LT phase, whereas the as-cast samples as well as the one annealed at 900°C contain exclusively the HT phase (Fig. 2). Other phases were not detected. The Rietveld refinements were performed with the MRIA program [42] using the crystallographic data obtained from the single crystal XRD experiments (Tables 1, 2) for orthorhombic HT-Ce₂Rh₂Ga and for monoclinic LT-Ce₂Rh₂Ga.

3.2 Crystal structures

The HT-Ce₂Rh₂Ga crystallizes with the orthorhombic La₂Ni₃-type structure [19], while the low-temperature polymorph adopts the monoclinic Pr₂Co₂Al (also known as Ca₂Ir₂Si) type [16, 17]. The non-f-electron counterpart La₂Rh₂Ga was found to crystallize with the orthorhombic La₂Ni₃-type structure.

The coordination polyhedra of all the atoms are presented in Fig. 3 and Fig. S2 in the Supplementary Materials. The environment of Ce atoms in the two polymorphs is rather similar and comprises six Rh, four Ga and five Ce atoms. The resulting polyhedron can be regarded as a derivative of a pentagonal prism centered on one basal face and on all side faces. In both structures, the Rh atom is coordinated by six cerium atoms and two gallium atoms in the form of a distorted square antiprism with two additional rhodium atoms capping the basal faces of the prism. Finally, the arrangement of the eight cerium atoms and four rhodium atoms around Ga results in a severely distorted icosahedron.

The Ce-Ce distances are ranging from 3.43 to 3.70 Å for the HT polymorph - within the similar range observed in the isostructural Ce₂Ru₂Al with $d_{\text{Ce-Ce}} = 3.32$ and 3.64 Å [25] - and from 3.61 to 3.71 Å for the LT one (Table 3). These distances correspond well to twice the metallic radius of this element ($r_{\text{Ce}} = 1.825$ Å [43]). Likewise, the interatomic distances Ce-Rh and Ce-Ga in HT modification are in the interval of corresponding values in the LT modification. Nevertheless, consideration of the Ga and Rh metallic radii ($r_{\text{Ga}} = 1.411$ Å and $r_{\text{Rh}} = 1.345$ Å [43]) highlights short Ce-Rh distances and rather elongated Ce-Ga ones. The Rh-Ga contacts of 2.56 Å in HT-Ce₂Rh₂Ga and from 2.58 to 2.61 Å in the LT-Ce₂Rh₂Ga are significantly smaller than the sum of the metallic radii, also suggesting a strong bonding between these elements. Opposite, more or less elongated Rh-Rh distances are observed and Ga atoms are well separated from each other and produce non-bonding contacts in both phases.

In the new compounds, the four Ga neighbors around each Ce atom form a slightly distorted CeGa₄ tetrahedron with Ce-Ga contacts being in the range of 3.34 – 3.39 Å and 3.30 – 3.35 Å for HT- and LT-Ce₂Rh₂Ga, respectively. Cerium centered gallium tetrahedra can be regarded as the

main common building blocks. In the HT-Ce₂Rh₂Ga, CeGa₄ tetrahedra are merged by edge-sharing with two neighboring ones forming rows alternating in a “checkerboard” pattern running along the *a*-axis (Fig. 4a). Each CeGa₄ tetrahedron has three more shared edges with adjacent rows.

The CeGa₄ tetrahedra are delimiting tetrahedral voids centered by Rh atoms (Fig. 4b). Thus the Ga environment of Rh atoms is a RhGa₄ tetrahedron which is severely distorted in contrast to that of Ce-centered. Within the Rh-centered tetrahedron, two Rh-Ga contacts are bonding – each of 2.555 Å - and two others are approximately 2 Å longer – 4.540 Å and 4.862 Å. Each RhGa₄ tetrahedron contacts with six neighbors by edge-sharing generating a 3D framework. The superposition of the Ce-centered tetrahedra and the Rh-centered tetrahedra nets results in a three-dimensional network by sharing triangular faces composed of Ga atoms (see Fig. 4c).

In the LT-Ce₂Rh₂Ga, the CeGa₄-tetrahedra framework is built by edge-sharing of each of the six edges of a CeGa₄ tetrahedron (Fig. 5a) which is delimiting octahedral voids centered by a Rh-Rh dumbbell (*d*_{Rh-Rh} = 2.75 Å). In this structure, each Rh atom resides in a distorted square-based pyramid RhGa₅ with Rh-Ga interatomic distances of 2.578 Å, 2.607 Å, 4.579 Å, 4.633 Å, and 4.668 Å. Two neighboring RhGa₅ pyramids share their basal faces to form a Rh₂Ga₆ octahedron (Fig. 5b). The resulting structure is produced by the CeGa₄- and Rh₂Ga₆-networks linked by the mutual triangular faces of the Ce-centered tetrahedra and of the Rh-double-centered octahedra (Fig. 5c).

3.3 Physical properties

LT-Ce₂Rh₂Ga. Figure 6 shows the variation of the Ce-molar magnetic susceptibility of LT-Ce₂Rh₂Ga with temperature on a logarithmic temperature scale. Below 400 K $\chi(T)$ assumes small values but follows a regular Curie-Weiss law, $\chi(T)=C/(T-\theta_P)$ down to 100 K as is shown by the line fitted to the experimental data (inset to Fig. 6). Here $C=N\mu_{\text{eff}}^2/Mk_B$ in terms of Avogadro's number *N*, the substance molar mass *M* and Boltzmann's constant *k_B*. The fit parameters are the Weiss temperature θ_P and the effective magnetic moment $\mu_{\text{eff}}^2=g_J^2J(J+1)$ in terms of the Landé factor $g_J=1+\{[J(J+1)+S(S+1)-L(L+1)]/[2J(J+1)]\}$ as function of the spin (*S*), orbital (*L*) and total (*J*) angular momentum quantum numbers. A good fit is achieved using an effective moment value of $\mu_{\text{eff}}=2.54 \mu_B \text{ Ce}^{-1}$. Interestingly, the obtained Weiss temperature is negative; $\theta_P=-30 \text{ K}$, which suggests dominant *antiferromagnetic* exchange in this compound. However, a steep and *ferromagnetic*-like increase in $\chi(T)$ is found upon cooling below 10 K. The point of steepest incline at this anomaly is marked with an arrow labelled as the Curie point $T_C=5.2 \text{ K}$ in Fig. 6.

The specific heat *C_p* per formula unit of LT-Ce₂Rh₂Ga is shown on a logarithmic temperature axis in the main panel of Fig. 7. Near room temperature $C_p \approx 125 \text{ J mol}_{\text{fu}}^{-1} \text{ K}^{-1}$ for this

compound which closely resembles the phenomenological Dulong-Petit value for a compound with five independent atoms in its formula unit [44]. C_p decreases steadily below room temperature but between 6 K and 5 K C_p rises sharply into a peak of nearly $20 \text{ J mol}_{\text{fu}}^{-1} \text{ K}^{-1}$ before decreasing further towards lower temperatures. The calculated configurational entropy S per mole Ce is shown in inset (a) of Fig. 7, where $S(T) = \int_0^T (C_p/T') dT'$. An entropy amount of $4.2 \text{ J mol}_{\text{Ce}}^{-1} \text{ K}$ is released at the phase transition which is somewhat lower than the value $R\ln(2)=5.76 \text{ J mol}^{-1} \text{ K}^{-1}$ attributable to long-range magnetic ordering out of a doublet ground state.

In inset (b) to Fig. 7 specific heat in the form $C_p(T)/T$ is plotted against the square of temperature. The linear behaviour above T_C enables to estimate the electronic contribution on account of the different temperature dependencies of the electronic γ and the lattice β specific heats; $C_p(T)/T = \gamma + \beta T^2$. The solid line on the data in inset (b) is the result of a least-square fit with $\gamma = 75 \text{ mJ mol}_{\text{Ce}}^{-1} \text{ K}^{-2}$ and $\beta = 0.547 \text{ mJ mol}_{\text{Ce}}^{-1} \text{ K}^{-4}$.

HT-Ce₂Rh₂Ga. Figure 8 (main panel) shows the per-mole Ce magnetic susceptibility of HT-Ce₂Rh₂Ga measured in a static field of 0.1 T. The line on the experimental points is the result of fitting the data to the Curie-Weiss law. Between 400 K and 200 K the experimental points may thus be described using an effective magnetic moment value of $2.54 \mu_B \text{ Ce}^{-1}$ and a Weiss temperature $\theta_p = -120 \text{ K}$. However, upon cooling below the predictable Curie-Weiss range, at a temperature labelled $T_N = 128.5 \text{ K}$ χ drops precipitously and continues to decrease losing about 25% of its magnitude at T_N when $\sim 80 \text{ K}$ is reached. Below this temperature χ rises again towards low temperatures. The shape of the anomaly in $\chi(T)$ at T_N is not unlike what may be expected at a paramagnetic-to-antiferromagnetic phase transition, which is corroborated by the dominant antiferromagnetic nature of the magnetic exchange obtained from the calculated negative value of the Weiss temperature for this compound. In the inset of Fig. 8 the region near T_N is shown on expanded scales. Between data collected while slowly cooling the sample (black symbols) and warming the sample (red symbols) a thermal hysteresis amounting to $\Delta T_N = 1 \text{ K}$ is found. Outside of the region of ΔT_N the warming and cooling data curves coincide. Figure 9 shows the results of magnetization measurements at a number of fixed temperatures. The three isotherms in panel (a) were collected at three temperatures close to the phase transition temperature. The field-dependent magnetization in this temperature region proceeds linearly in field up to 7 T. The magnetic moment extracted from magnetization measurements even at low temperature and deep into the ordered region is small – see Fig. 9(b). An applied field of 9 T yields only $0.34 \mu_B \text{ Ce}^{-1}$ for the sample at 1.7 K. It is noteworthy, however, that correlated electron Ce-based compounds often yield only small magnetization values [45, 46].

Finally, we turn to the specific heat of HT-Ce₂Rh₂Ga as illustrated in the main panel of Fig. 10 on a per-chemical formula unit basis. Below room temperature we notice that C_p is nearly constant at a value close to the Dulong-Petit value for this compound. In the Debye model of the specific heat of solids this value is achieved when the substance is at a temperature suitably higher than its Debye temperature θ_D . At 130 K however, the monotonous behavior in $C_p(T)$ ceases where C_p rises very sharply and achieves 424 J mol_{fu}⁻¹ K⁻¹ at 127.5 K. In the inset of Fig. 10 we cast the specific heat data below 20 K in the form $C_p(T)/(T)$ against the square of temperature. The line on the experimental points is drawn with $\gamma=172.5$ mJ mol_{Ce}⁻¹ K⁻¹ and $\beta=1.217 \times 10^{-3}$ mJ mol_{Ce}⁻¹ K⁻⁴. By contrast, in the specific heat of the comparable nonmagnetic compound La₂Rh₂Ga (see Fig. 11a) there are no anomalies observed below room temperature, as would be expected for a simple metal. For La₂Rh₂Ga the Sommerfeld coefficient is found to be $\gamma=13.45$ mJ mol_{La}⁻¹ K⁻² according to the least-squares fit shown in panel (b) of Fig. 11.

The unusual behavior of HT-Ce₂Rh₂Ga at 128.5 K prompted us to search for a possible crystal structure phase transition. The first attempts to determine structural changes in the transition through $T_N=128$ K using single crystal X-ray diffraction showed that the structure changes are too small to be reliably described quantitatively. Changes in cell dimensions and cell volume as well as the appearance of a small monoclinic distortion when cooling a single crystal of HT-Ce₂Rh₂Ga from room temperature down to 80 K are presented in Figure S3 (Supplementary materials). Further crystal structure determination was not possible due to the twinning of the crystals induced by the structural transition.

4 Discussion

The two new Ce-based compounds LT-Ce₂Rh₂Ga and HT-Ce₂Rh₂Ga show contrasting behaviours despite being alike in their chemical compound formulas. In both structures Ce atoms occupy a unique crystallographic site however in LT-Ce₂Rh₂Ga it is a general position $8f$ (site symmetry 1) and in HT-Ce₂Rh₂Ga it is a special position $8f$ (site symmetry m). Magnetically, both compounds can be described in terms of the full trivalent magnetic state of the Ce ion over a wide range below room temperature, which makes both compounds amenable to magnetic order. In LT-Ce₂Rh₂Ga the Ce ions order in a spin arrangement at a temperature of 5.2 K that imparts a ferromagnetic character to its temperature-dependent magnetic susceptibility as well as its field-dependent magnetization. This magnetic phase transition temperature is typically in the range of many cerium-based compounds. The single $4f$ -electron of cerium in its trivalent state being predisposed to an antiferromagnetic on-site Kondo exchange in metals, however, means that by comparison ferromagnetic order in cerium intermetallic compounds is much less ubiquitous than antiferromagnetic order.

Taken together, the results of magnetic susceptibility and specific heat for the phase transition found in this study on the compound HT-Ce₂Rh₂Ga bear the signatures of antiferromagnetic order, but at the extraordinary high phase transition temperature of 128.5 K. With the present state of investigation and results available on this compound we cannot rule out the possibility of a crystal structure modification accompanying the magnetic phase transition at T_N . This phase transition is temperature hysteretic furthermore which is unusual since fluctuations in the order parameter is a common feature of magnetic order driven by an anti-parallel spin arrangement.

In conclusion, the novel Ce₂Rh₂Ga intermetallics crystallize in two polymorphs adopting rather unusual structure-types: an orthorhombic ordered La₃Ni₂-type for samples annealed above 867°C and a monoclinic Pr₂Co₂Al-type for samples annealed below this temperature. Both structure types can be built from CeGa₄ cerium centered gallium tetrahedral bricks. Both allotropes show phase transitions of a magnetic nature and further studies are needed to determine the order parameter. In HT-Ce₂Rh₂Ga in particular it would be interesting to clarify what property of the material is driving the temperature hysteresis that accompanies the magnetic ordering.

Acknowledgements

AMS thanks the URC/FRC of UJ and the SA NRF (93549) for generous financial assistance, and the Max Planck Institute CPfS in Dresden for their hospitality where parts of this research were conducted. This study was supported by the Russian Foundation for Basic Research (Grant No 18-03-00656a and 19-03-00135).

References

1. M. Giovannini, H. Michor, E. Bauer, G. Hilscher, P. Rogl, R. Ferro, Structural chemistry, magnetism and thermodynamic properties of R₂Pd₂In, J. Alloys Compd. 280 (1998) 26-38. [https://doi.org/10.1016/S0925-8388\(98\)00723-3](https://doi.org/10.1016/S0925-8388(98)00723-3).
2. M. Lukachuk, R. Pöttgen, Intermetallic compounds with ordered U₃Si₂ or Zr₃Al₂ type structure-crystal chemistry, chemical bonding and physical properties, Z. Kristallogr. 218 (2003) 767-787. <https://doi.org/10.1524/zkri.218.12.767.20545>.
3. R. Pöttgen, U.C. Rodewald, Rare Earth–Transition Metal–Plumbides, in: K.A. Gschneidner Jr., L. Eyring (Eds.), Handbook on the Physics and Chemistry of Rare Earths, vol. 38, Elsevier Science Publishers B V, Amsterdam, 2008, pp. 55-103. [https://doi.org/10.1016/S0168-1273\(07\)38002-1](https://doi.org/10.1016/S0168-1273(07)38002-1).

4. D. Kaczorowski, P. Rogl, K. Hiebl, Magnetic behavior in a series of cerium ternary intermetallics: $\text{Ce}_2\text{T}_2\text{In}$ (T=Ni, Cu, Rh, Pd, Pt, and Au), *Phys. Rev. B* 54 (1996) 9891. .
<https://doi.org/10.1103/physrevb.54.9891>.
5. B. Chevalier, J. García Soldevilla, J.C. Gómez Sal, J.M. Barandiarán, J. Etourneau, Magnetoresistivity of the antiferromagnetic Kondo stannide $\text{Ce}_2\text{Ni}_2\text{Sn}$, *J. Magnetism and Magnetic Materials* 196-197 (1999) 878-879.
[https://doi.org/10.1016/S0304-8853\(98\)00968-8](https://doi.org/10.1016/S0304-8853(98)00968-8).
6. D. Niepmann, R. Pöttgen, B. Künnen, G. Kotzyba, $\text{Ce}_2\text{Ni}_2\text{Cd}$ - a new intermediate-valent cerium compound, *J. Solid State Chem.* 150 (2000) 139-144.
<https://doi.org/10.1006/jssc.1999.8567>.
7. E.V. Sampathkumaran, K.K. Iyer, N. Mohapatra, S. Rayaprol, R. Pöttgen, Heavy fermion behaviour in $\text{Ce}_2\text{Ni}_{1.88}\text{Cd}$, *Z. Naturforsch.* 62b (2007) 891 – 895.
<https://doi.org/10.1515/znb-2007-0703>.
8. D. Kaczorowski, P. Rogl, Magnetic behaviour in CeNiGa_2 and $\text{Ce}_2\text{Ni}_2\text{Ga}$, *Acta Physica Polonica* 92 (1997) 289-293.
9. C. Geibel, U. Klinger, B. Buschinger, M. Weiden, G. Olesch, F. Thomas, F. Steglich, $\text{Yb}_2\text{Ni}_2\text{Al}$: A prototypical Yb-based heavy-fermion system, *Physica B: Cond. Matter* 223–224 (1996) 370-372.
[https://doi.org/10.1016/0921-4526\(96\)00125-1](https://doi.org/10.1016/0921-4526(96)00125-1).
10. T. Muramatsu, T. Kanemasa, T. Kagayama, K. Shimizu, Y. Aoki, H. Sato, M. Giovannini, P. Bonville, V. Zlatic, I. Aviani, R. Khasanov, C. Rusu, A. Amato, K. Mydeen, M. Nicklas, H. Michor, E. Bauer, Reentrant quantum criticality in $\text{Yb}_2\text{Pd}_2\text{Sn}$, *Phys. Rev. B* 83 (2011) 180404(R).
<https://doi.org/10.1103/PhysRevB.83.180404>.
11. W. Rieger, H. Nowotny, F. Benesovsky, Die Kristallstruktur von Mo_2FeB_2 , *Monatsh. Chem.* 95 (1964) 1502-1503.
<https://doi.org/10.1007/BF00901704>.
12. R. Pöttgen, $\text{Er}_2\text{Au}_2\text{Sn}$ and other Ternary Rare Earth Metal Gold Stannides with Ordered Zr_3Al_2 -Type Structure, *Z. Naturforsch. B* 49 (1994) 1309–1313.
<https://doi.org/10.1515/znb-1994-1001>.
13. P. Gravier, F. Mirambet, B. Chevalier, F. Weill, L. Fournès, D. Laffargue, F. B. Vigneron, J.R. Etourneau, Crystal structure of $\text{U}_2\text{Pt}_2\text{Sn}$: a new derivative of the tetragonal U_3Si_2 -type structure, *J. Mater. Chem.* 4 (1994) 1893-1895.
<https://doi.org/10.1039/JM9940401893>.
14. W. Rieger, H. Nowotny, F. Benesovsky, Die Kristallstruktur von W_2CoB_2 und isotypen Phasen, *Monatsh. Chem.* 97 (1966) 378-382.

<https://doi.org/10.1007/BF00905254>.

15. H.J. Becher, K. Krogmann, E. Peisker, Über das ternäre Borid Mn_2AlB_2 , Z. Anorg. Allg. Chem. 344 (1966) 140–147.

<https://doi.org/10.1002/zaac.19663440304>

16. M. Pani, F. Merlo, M.L. Fornasini, Structure and transport properties of the R_2Co_2Al compounds ($R = Pr, Nd, Sm, Gd, Tb, Dy, Ho, Er, Tm, Y$), Z. Kristallogr. 217 (2002) 415–419.

<https://doi.org/10.1524/zkri.217.7.415.23677>.

17. S. Schoolaertm, W. Jung, Synthese und Kristallstrukturen der Calcium-Iridiumsilicide $Ca_3Ir_4Si_4$ und Ca_2Ir_2Si , Z. Anorg. Allg. Chem. 628 (2002) 1806–1810.

[https://doi.org/10.1002/1521-3749\(200208\)628:8<1806::AID-ZAAC1806>3.0.CO;2-E](https://doi.org/10.1002/1521-3749(200208)628:8<1806::AID-ZAAC1806>3.0.CO;2-E).

18. F. Tappe, R.-D. Hoffmann, M. Eul, R. Pöttgen, Dimorphic Nd_2Cu_2Cd - structures and magnetic properties of RE_2Cu_2Cd ($RE = Ce, Pr, Nd$), Z. Kristallogr. 226 (2011) 201–213.

<https://doi.org/10.1524/zkri.2011.1297>.

19. J.H.N. van Vucht, K.H.J. Buschow, The crystal structure of La_2Ni_3 , J. Less-Common Met. 46 (1976) 133 – 138.

[https://doi.org/10.1016/0022-5088\(76\)90186-7](https://doi.org/10.1016/0022-5088(76)90186-7).

20. M. Pustovoychenko, V. Svitlyk, Ya. Kalychak, Orthorhombic La_2Ni_2In - A new intergrown CsCl- and AlB_2 -type slabs, Intermetallics 24 (2012) 30–32.

<https://doi.org/10.1016/j.intermet.2012.01.007>.

21. I. Doverbratt, S. Ponou, Y. Zhang, S. Lidin, G. J. Miller, Linear Metal Chains in Ca_2M_2X ($M = Pd, Pt$; $X = Al, Ge$): Origin of the Pairwise Distortion and Its Role in the Structure Stability, Chem. Mater. 27 (2015) 304–315.

<https://doi.org/10.1021/cm503985h>.

22. F. Stegemann, C. Benndorf, R. St.Touzani, B. P.T.Fokwa, O. Janka, Experimental and theoretical investigations of the polar intermetallics $SrPt_3Al_2$ and Sr_2Pd_2Al , J. Solid State Chem., 242(2016), 143–150.

<https://doi.org/10.1016/j.jssc.2016.07.019>

23. V. Stotskyi, S. Pukas, R. Gladyshevskii, Crystal structure of a solid solution in the Mg–Pd–Al system, Chem. Met. Alloys 12 (2019) 29–32.

<https://doi.org/10.30970/cma12.0391>

24. M. Dzevenkoa, K. Miliyanchuka, Ya. Filinchuk, O. Stelmakhovich, L. Akselrud, L. Havela, Ya. Kalychak, Large hydrogen capacity in hydrides R_2Ni_2In-H ($R = La, Ce, Pr, Nd$) with new structure type, J.Alloys and Compd., 477 (2009) 182–187. <https://doi.org/10.1016/j.jallcom.2008.10.042>

<https://doi.org/10.1016/j.jallcom.2008.10.042>

25. E.V. Marushina, D. Kaczorowski, E.V. Murashova, Zh M. Kurenbaeva, A.V. Gribanov, Crystal structure and unstable valence in a novel intermetallic phase $\text{Ce}_2\text{Ru}_2\text{Al}$, J. Alloys and Compd.. 650(2015) 654–657. <https://doi.org/10.1016/j.jallcom.2015.08.027>
26. T. Mahon, E. Gaudin, B. Vignolle, G. Ballon, B. Chevalier, et al., $\text{R}_2\text{Co}_{3-x}\text{Si}_x$ ($\text{R} = \text{Pr}, \text{Nd}, \text{Sm}, \text{Gd}$) and $\text{R}_2\text{Ni}_{3-x}\text{Si}_x$ ($\text{R} = \text{Gd-Er}$), new series of La_2Ni_3 -type phases. J. Alloys and Compd., 737(2018)377-386.
<https://doi.org/10.1016/j.jallcom.2017.12.013>.
27. B. Heying, U.Ch. Rodewald, B. Chevalier, R. Pöttgen, The Stannides $\text{RE}_2\text{Ni}_2\text{Sn}$ ($\text{RE} = \text{Pr}, \text{Ho}, \text{Er}, \text{Tm}$) - Structural Transition from the $\text{W}_2\text{B}_2\text{Co}$ to the $\text{Mo}_2\text{B}_2\text{Fe}$ Type as a Function of the Rare Earth Size, Z. Naturforsch. 68b (2013) 10 - 16.
<https://doi.org/10.5560/znb.2013-2296>.
28. G. Heymann, B. Heying, U.C. Rodewald, B. Chevalier, H. Huppertz, R. Pöttgen, High-pressure phases of $\text{Tb}_2\text{Ni}_2\text{Sn}$ and $\text{Dy}_2\text{Ni}_2\text{Sn}$, Monatsh. Chem. 145 (2014) 863-867.
<https://doi.org/10.1007/s00706-014-1179-8>.
29. F. Hulliger, On tetragonal $\text{M}_2\text{Au}_2\text{In}$ and related compounds, J. Alloys Compd. 1996, 232, 160-164.
[https://doi.org/10.1016/0925-8388\(95\)01925-1](https://doi.org/10.1016/0925-8388(95)01925-1).
30. R. Pöttgen, Ternary Rare Earth Metal Gold Stannides and Indides with Ordered U_3Si_2 and Zr_3Al_2 -Type Structure, Z. Naturforsch. 49b (1994) 1525-1530.
<https://doi.org/10.1515/znb-1994-1112>.
31. Ya.M. Kalychak, V.I. Zaremba, V.M. Baranyak, P.Yu. Zavali, V.A. Bruskov, L.V. Sysa, O.V. Dmytrakh, The crystal structure of the compounds $\text{R}_2\text{Ni}_2\text{In}$, $\text{R}_2\text{Ni}_{2-x}\text{In}$ and $\text{R}_2\text{Cu}_2\text{In}$ ($\text{R} = \text{La}, \text{Ce}, \text{Pr}, \text{Nd}, \text{Sm}, \text{Gd}, \text{Tb}, \text{Dy}, \text{Ho}, \text{Er}, \text{Tm}, \text{Lu}, \text{Y}$), Sov. Izv. Acad. Nauk Inorg. Mat. 26 (1990), 94-96.
32. T. Fickenscher, U.C. Rodewald, D. Niepmann, R. Mishra, M. Eschen, R. Pöttgen, The Mo_2FeB_2 - and Mn_2AlB_2 -Type Modifications of $\text{RE}_2\text{Ni}_2\text{Cd}$ ($\text{RE} = \text{La}, \text{Pr}, \text{Nd}, \text{Sm}, \text{Tb}, \text{Dy}$), Z. Naturforsch. 60b (2005) 271 - 276.
<https://doi.org/10.1515/znb-2005-0306>.
33. P. Estrela, L.C.J. Pereira, A. de Visser, F.R. de Boer, M. Almeida, M. Godinho, J. Rebizant, J.C. Spirle, Structural, magnetic and transport properties of single-crystalline $\text{U}_2\text{Pt}_2\text{In}$, J. Phys.: Condens. Matter 10 (1998) 9465-9475.
<https://doi.org/10.1088/0953-8984/10/42/012>.
34. M. Dzevenko, K. Miliyanchuka, Ya. Filinchuk, O. Stelmakhovych, L. Akselrud, L. Havela, Ya. Kalychak, Large hydrogen capacity in hydrides $\text{R}_2\text{Ni}_2\text{In-H}$ ($\text{R} = \text{La}, \text{Ce}, \text{Pr}, \text{Nd}$) with new

- structure type, J. Alloys Compd. 477 (2009) 182-187.
<https://doi.org/10.1016/j.jallcom.2008.10.042>.
35. F. Canepa, M. Napolitano, M.L. Fornasini, F. Merlo, Structure and magnetism of $\text{Gd}_2\text{Co}_2\text{Ga}$, $\text{Gd}_2\text{Co}_2\text{Al}$ and $\text{Gd}_{14}\text{Co}_3\text{In}_{2.7}$, J. Alloys Compd. 345 (2002) 42–49.
[https://doi.org/10.1016/S0925-8388\(02\)00395-X](https://doi.org/10.1016/S0925-8388(02)00395-X)
36. O.M. Sichevich, Ternary intermetallic compound with the La_2Ni_3 structure in the Gd-Co-Ga system, Dopov. Akad. Nauk Ukr. RSR, Ser. B: 12 (1984) 46-48 (in Ukrainian).
36. A.V. Morozkin, O. Isnard, R. Nirmala, S.K. Malik, Mo_2NiB_2 -type $\{\text{Gd}, \text{Tb}, \text{Dy}\}_2\text{Ni}_{2.35}\text{Si}_{0.65}$ and La_2Ni_3 -type $\{\text{Dy}, \text{Ho}\}_2\text{Ni}_{2.5}\text{Si}_{0.5}$ compounds: Crystal structure and magnetic properties, J. Solid State Chem. 225 (2015) 368-377.
<https://doi.org/10.1016/j.jssc.2015.01.017>.
37. A. M. Strydom, A. Tursina, Unusual order in the new compound $\text{Ce}_2\text{Rh}_2\text{Ga}$, Book of abstract SCTE-18, 18th International conference on solid compounds of transition elements; Vienna, Austria, 25-29 March; 2018, 83.
38. G.M. Sheldrick, A short history of SHELX, Acta Crystallogr. A64 (2008) 112-122.
<https://doi.org/10.1107/S0108767307043930>.
39. F. Hulliger, On new rare-earth compounds LnIrGa and LnRhGa , J. Alloys Compd. 239 (1996) 131-134.
[https://doi.org/10.1016/0925-8388\(96\)02262-1](https://doi.org/10.1016/0925-8388(96)02262-1).
40. B. Chevalier, B. Heying, U. Ch. Rodewald, C. P. Sebastian, E. Bauer, R. Pöttgen, Hydrogenation of the $\text{Ce}(\text{Rh}_{1-x}\text{Ir}_x)\text{Ga}$ System: Occurrence of Antiferromagnetic Ordering in the Hydrides $\text{Ce}(\text{Rh}_{1-x}\text{Ir}_x)\text{GaH}_{1.8}$, Chem.Mater., 19 (2007) 3052-3060. <https://doi.org/10.1021/cm0705338>
41. J. Goraus, A. Ślebarski, M. Fijałkowski, Electronic and thermal properties of non-magnetic CeRhGa , J. Alloys Compd. 509 (2011) 3735-3739. <https://doi.org/10.1016/j.jallcom.2010.12.183>
42. V.B. Zlokazov, V.V. Chernyshev, MRIA - a program for a full profile analysis of powder multiphase neutron-diffraction time-of-flight (direct and Fourier) spectra, J. Appl. Crystallogr. 25 (1992) 447-451.
<https://doi.org/10.1107/S0021889891013122>.
43. E. Teatum, K. Gschneidner, J. Waber, Compilation of calculated data useful in predicting metallurgical behavior of the elements in binary alloy systems, LA-2345, Los Alamos Scientific Laboratory (1960).
44. A.T. Petit ; P.L Dulong, Recherches sur quelques points importants de la Théorie de la Chaleur; Ann: Chim: Phys; 10 (1819) 395-413.

45. O. Janka, O. Niehaus, R. Pöttgen, B. Chevalier, Cerium intermetallics with TiNiSi-type structure, *Z. Naturforsch.* 71b (2016) 737-764.
46. R. Pöttgen, B Chevalier, Cerium intermetallics with ZrNiAl-type structure – a review, *Z. Naturforsch.* 70b (2015) 289-304.

Table 1. Selected single-crystal data collection and structure refinement parameters for La₂Rh₂Ga, HT-Ce₂Rh₂Ga, and LT-Ce₂Rh₂Ga.

Empirical formula	La ₂ Rh ₂ Ga	HT-Ce ₂ Rh ₂ Ga	LT-Ce ₂ Rh ₂ Ga
Molar mass, g·mol ⁻¹	553.36	555.78	
Space group	<i>Cmce</i> (64)	<i>Cmce</i> (64)	<i>C</i> 2/c (15)
Structure type	La ₂ Ni ₃	La ₂ Ni ₃	Pr ₂ Co ₂ Al
<i>a</i> (Å)	5.9251(17)	5.851(2)	10.0903(6)
<i>b</i> (Å)	9.8402(17)	9.618 (2)	5.6041(3) β=104.995(3)°
<i>c</i> (Å)	7.5019(14)	7.487 (2)	7.8153(4)
Cell volume (Å ³)	437.39(17)	421.3(2)	426.88(4)
<i>Z</i>	4	4	4
D calc (g·cm ⁻³)	8.403	8.762	8.648
Abs. coeff μ (mm ⁻¹)	17.046	18.437	34.464
Radiation (Å)	AgKα, 0.56087	AgKα, 0.56087	MoKα, 0.71073
Index range	-8 ≤ <i>h</i> ≤ 8, 0 ≤ <i>k</i> ≤ 14, 0 ≤ <i>l</i> ≤ 11	0 ≤ <i>h</i> ≤ 11, -19 ≤ <i>k</i> ≤ 0, -15 ≤ <i>l</i> ≤ 15	-16 ≤ <i>h</i> ≤ 16, 0 ≤ <i>k</i> ≤ 9, 0 ≤ <i>l</i> ≤ 13
Θ range	3.27 – 24.5	3.34° - 34.96°	4.18° - 36.53°
Number of measured reflections	803	983	1060
Number of reflections with <i>I</i> ≥ 2σ(<i>I</i>)	361	597	937
Number of refined parameters	17	17	25
GooF on <i>F</i> ²	1.116	0.972	1.088
<i>R</i> [<i>F</i> ² > 2σ(<i>F</i> ²)]	0.0310	0.0389	0.0239
<i>wR</i> (<i>F</i> ²)	0.0843	0.0641	0.0537

Table 2. Atomic coordinates and equivalent isotropic displacement parameters U_{eq} (\AA^2) for $\text{La}_2\text{Rh}_2\text{Ga}$, HT- $\text{Ce}_2\text{Rh}_2\text{Ga}$, and LT- $\text{Ce}_2\text{Rh}_2\text{Ga}$.

Atom	Wyckoff site	x/a	y/b	z/c	U_{eqv}
$\text{La}_2\text{Rh}_2\text{Ga}$					
La	$8f$	0	0.33857(4)	0.09757(6)	0.0132(2)
Rh	$8e$	1/4	0.09407(5)	1/4	0.0146(2)
Ga	$4a$	0	0	0	0.0128(3)
HT-$\text{Ce}_2\text{Rh}_2\text{Ga}$					
Ce	$8f$	0	0.33904(4)	0.09881(6)	0.0123(1)
Rh	$8e$	1/4	0.09769(6)	1/4	0.0143 (2)
Ga	$4a$	0	0	0	0.0118(2)
LT-$\text{Ce}_2\text{Rh}_2\text{Ga}$					
Ce	$8f$	0.35324(2)	0.14759(4)	0.35191(3)	0.01041(7)
Rh	$8f$	0.13144(3)	0.13464(5)	0.00765(4)	0.01100(8)
Ga	$4e$	0	0.1398(2)	1/4	0.0098(2)

Table 3. Interatomic distances (Å) in the HT- and LT- Ce₂Rh₂Ga

HT- Ce ₂ Rh ₂ Ga			LT- Ce ₂ Rh ₂ Ga					
Atom	To atom	<i>d</i>	Atom	To atom	<i>d</i>	Atom	To atom	<i>d</i>
Ce	2 Rh	2.9680(8)	Ce	Rh	2.9310(4)	Rh	Ga	2.5781(3)
	2 Rh	3.0545(7)		Rh	3.0227(4)		Ga	2.6070(5)
	2 Rh	3.1000(8)		Rh	3.0227(4)		Rh	2.7494(6)
	Ga	3.3438(7)		Rh	3.0666(4)		Ce	2.9310(4)
	Ga	3.3793(8)		Rh	3.1040(4)		Ce	3.0137(4)
	2 Ga	3.391(1)		Rh	3.2252(4)		Ce	3.0227(4)
	Ce	3.432(1)		Ga	3.3028(3)		Rh	3.0270(6)
	2 Ce	3.699(1)		Ga	3.3235(6)		Ce	3.0667(4)
	2 Ce	3.699(2)		Ga	3.3965(6)		Ce	3.1040(4)
Rh	2 Ga	2.5546(5)		Ga	3.4455(3)		Ce	3.2252(4)
	2 Rh	2.925 (2)		Ce	3.6072(3)	Ga	2 Rh	2.5782(4)
	2 Ce	2.9680(8)		Ce	3.6073(3)		2 Rh	2.6071(5)
	2 Ce	3.0545(7)		Ce	3.6495(5)		2 Ce	3.3028(3)
	2 Ce	3.1000(8)		Ce	3.6759(5)		2 Ce	3.3235(6)
Ga	4 Rh	2.5546(5)		Ce	3.7081(5)		2 Ce	3.3965(6)
	2 Ce	3.3438(8)					2 Ce	3.4455(3)
	2 Ce	3.3793(8)						
	4 Ce	3.391 (1)						

Figure Captions

Fig. 1 DTA curve of the annealed at 700°C sample (the arrows show the course of temperature change).

Fig. 2 Rietveld refined X-ray diffraction patterns for (up) HT-Ce₂Rh₂Ga ($\chi^2 = 1.78$, $R_p = 0.024$, $R_{exp} = 0.022$) and (down) LT-Ce₂Rh₂Ga ($\chi^2 = 3.69$, $R_p = 0.024$, $R_{exp} = 0.015$). The experimental diffraction profile is indicated by black dots. The calculated diffraction profile is shown as the upper blue line, the difference profile is shown as the bottom red line and the vertical bars correspond to the calculated Bragg positions.

Fig.3. Coordination polyhedra of the three atoms in the crystal structure of HT-Ce₂Rh₂Ga (upper row) and LT-Ce₂Rh₂Ga (bottom row). Ce-atoms are drawn as large green balls, Rh-atoms as small blue ball, and Ga-atoms as middle size pink balls.

Fig. 4. (a) CeGa₄ and (b) RhGa₄ tetrahedra arrangement in the unit cell of HT-Ce₂Rh₂Ga. (c) The packing of the CeGa₄ and RhGa₄ tetrahedra. CeGa₄ tetrahedra are highlighted in green, RhGa₄ tetrahedra are highlighted in blue.

Fig. 5. (a) CeGa₄ tetrahedra and (b) double centered Rh octahedra arrangement in the unit cell of LT-Ce₂Rh₂Ga. (c) The packing of the CeGa₄ tetrahedra and Rh₂Ga₆ octahedra. CeGa₄ tetrahedra are highlighted in green. Rh₂Ga₆-octahedra are emphasized in blue.

Fig. 6. (main panel) Semi-log plot of dc-magnetic susceptibility per mole Ce of LT-Ce₂Rh₂Ga measured in a static applied field of 0.1 T, with the arrow marking the paramagnetic-to-ferromagnetic phase transition temperature T_C . (inset) Inverse susceptibility against temperature. The solid line is a Curie-Weiss fit to the data as explained in the text.

Fig. 7. (main panel) Semi-log plot of the specific heat C_p per mole of Ce of LT-Ce₂Rh₂Ga. The arrow indicates the ferromagnetic phase transition temperature. Dashed line is a guide to the eye connecting the experimental points. Inset (a): Calculated entropy per mole of Ce. Inset (b): Specific heat in the form $C_p(T)/T$ against the square of temperature. The dashed line is a guide to the eye. Solid line illustrates a fit to extract the Sommerfeld coefficient $\gamma = 75 \text{ mJ mol}_{\text{Ce}}^{-1} \text{ K}^{-2}$.

Fig. 8. (main panel) Magnetic dc-susceptibility of HT-Ce₂Rh₂Ga measured in a static applied field of 0.1 T. The solid line on the data is obtained through a Curie-Weiss fit. The dashed line illustrates the continuation of the Curie-Weiss fit below the fitted temperature range which is intercepted at the phase transition marked T_N at 128.5 K. (inset) Magnetic susceptibility on expanded scales near T_N shows the temperature hysteretic behaviour between data obtained during cooling (black symbols) and warming (red symbols) of the sample.

Fig. 9. dc-Magnetization per Ce atom of HT-Ce₂Rh₂Ga at temperatures (a) close to T_N and (b) at low temperature. The magnetization is linear in field at all investigated temperatures except for the $T=1.70$ K isotherm where the high-field region permits to calculate a saturation magnetization of $0.19 \mu_B/\text{Ce}$.

Fig. 10. (main panel) Temperature dependence of specific heat per formula unit of HT-Ce₂Rh₂Ga. The dashed line is a guide to the eye to connect the data points through the sharp phase transition marked by an arrow at $T_N=128.5$ K. (inset) Specific heat per mole of Ce of HT-Ce₂Rh₂Ga in the form $C_p(T)/T$ plotted against the square of temperature. The solid line on the data is a fit to extract the electronic specific heat coefficient $\gamma=172.5 \text{ mJ mol}_{\text{Ce}}^{-1}\text{K}^{-2}$. An upturn of unknown origin is found to occur in $C_p(T)/T$ below about 7 K.

Fig. 11. (a) Specific heat of the Pauli-paramagnetic compound La₂Rh₂Ga over a wide range of temperature. (b) Specific heat in the form $C_p(T)/T$ against the square of temperature. A value $\gamma=13.45 \text{ mJ mol}_{\text{La}}^{-1} \text{K}^{-2}$ is obtained for the Sommerfeld coefficient as illustrated by the solid line on the data points.

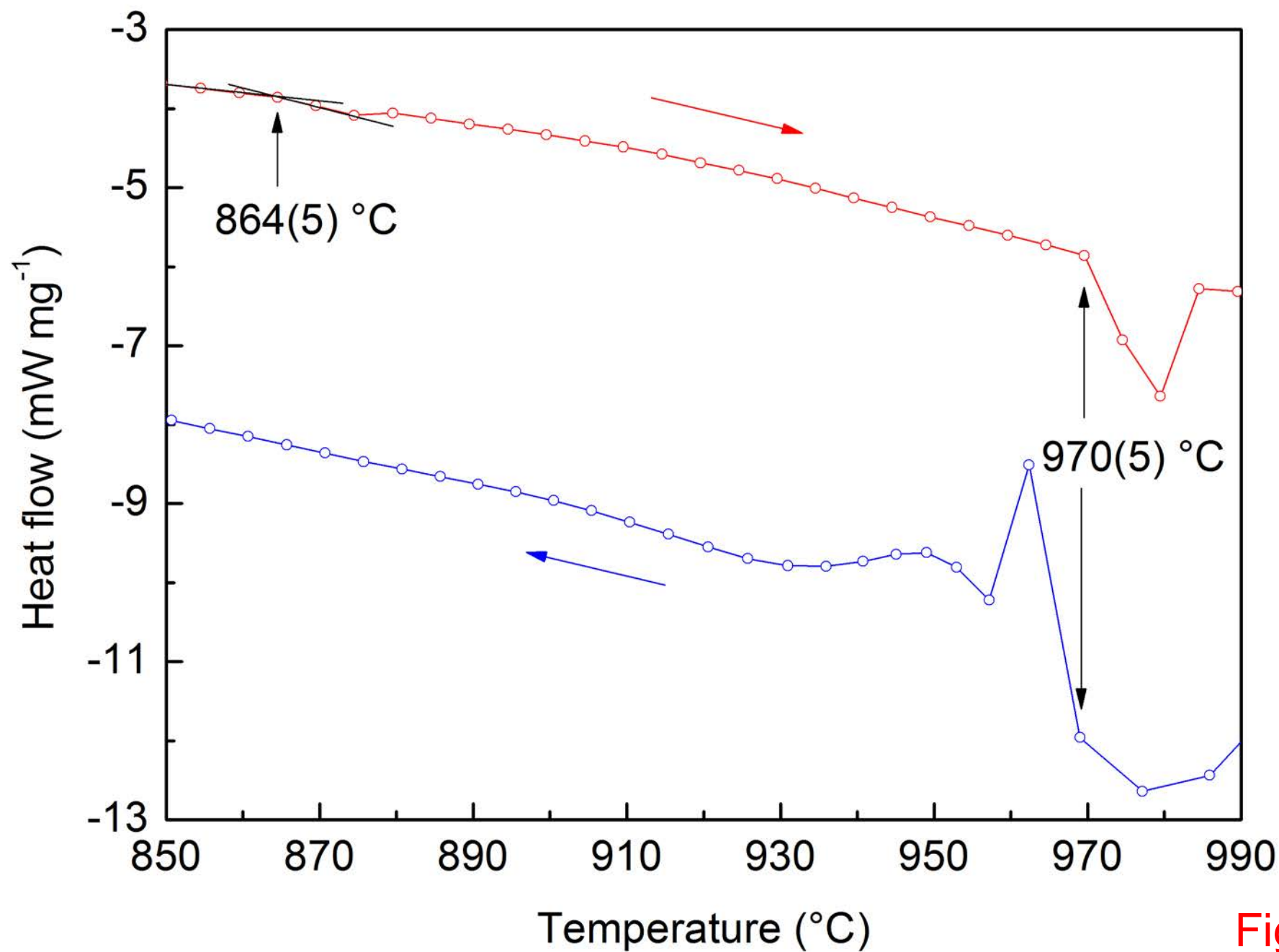


Figure 1

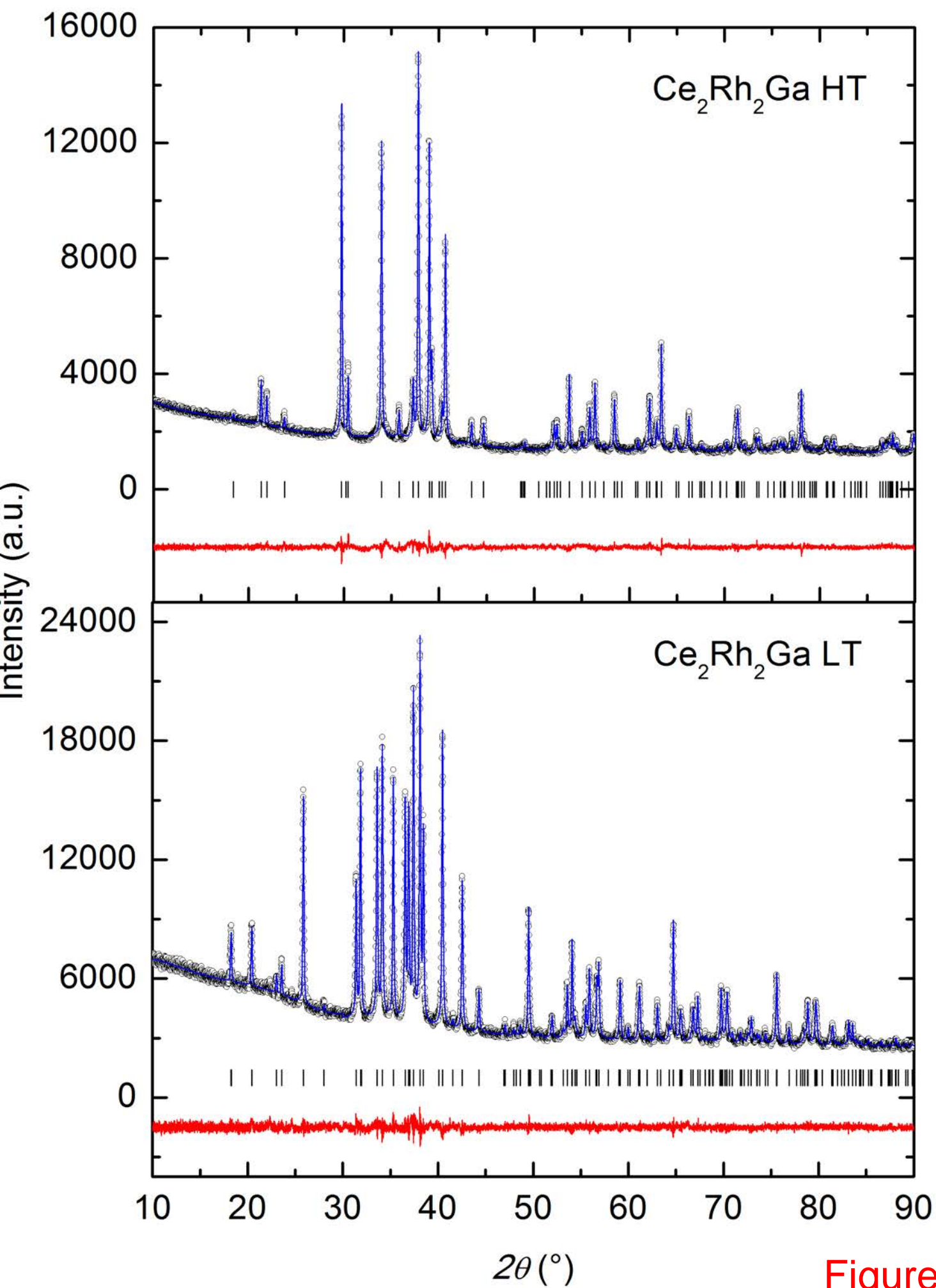
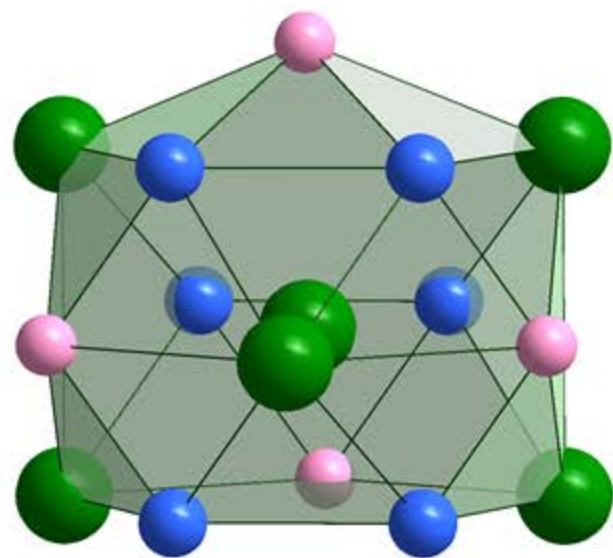
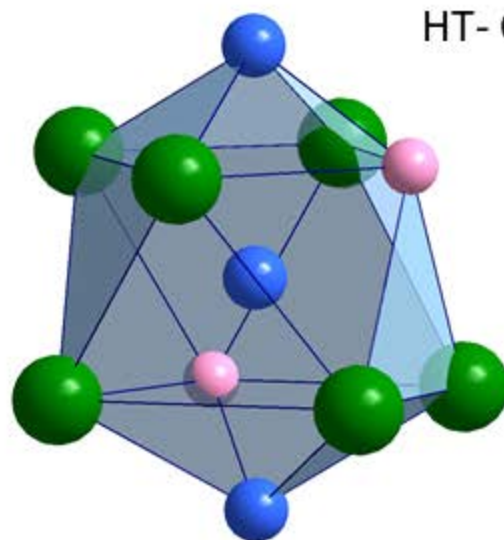


Figure 2

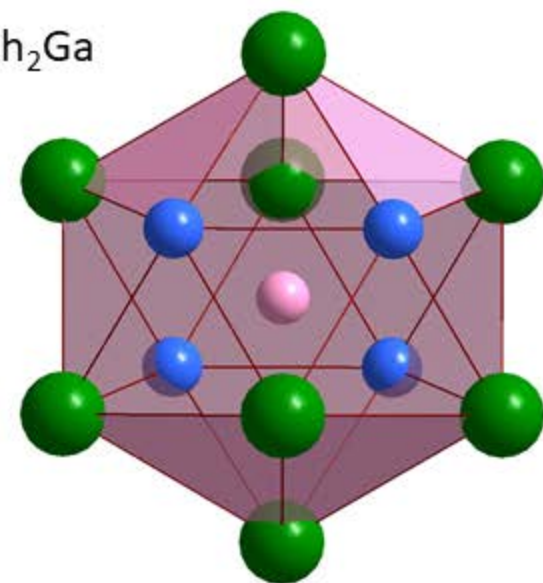


Ce

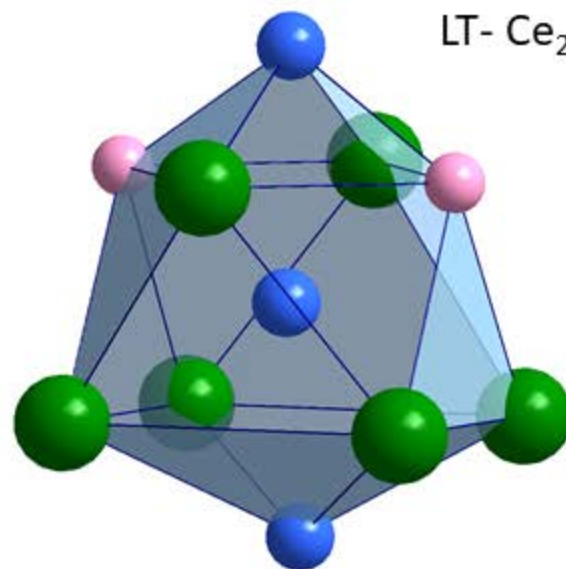
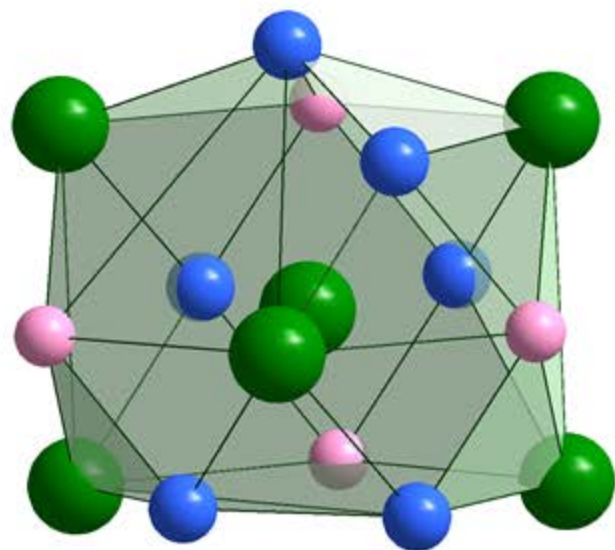


Rh

HT- $\text{Ce}_2\text{Rh}_2\text{Ga}$



Ga



LT- $\text{Ce}_2\text{Rh}_2\text{Ga}$

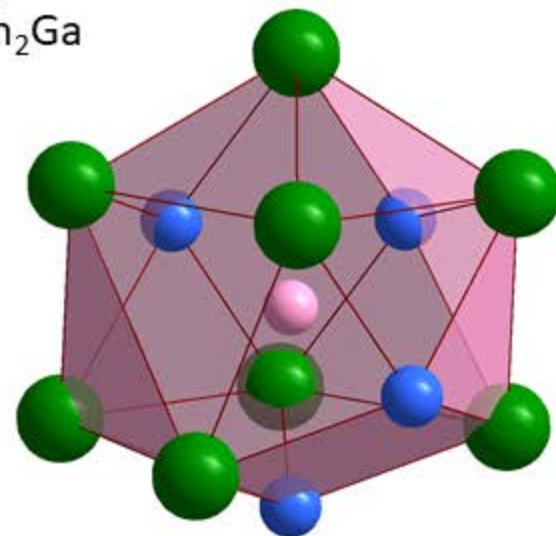
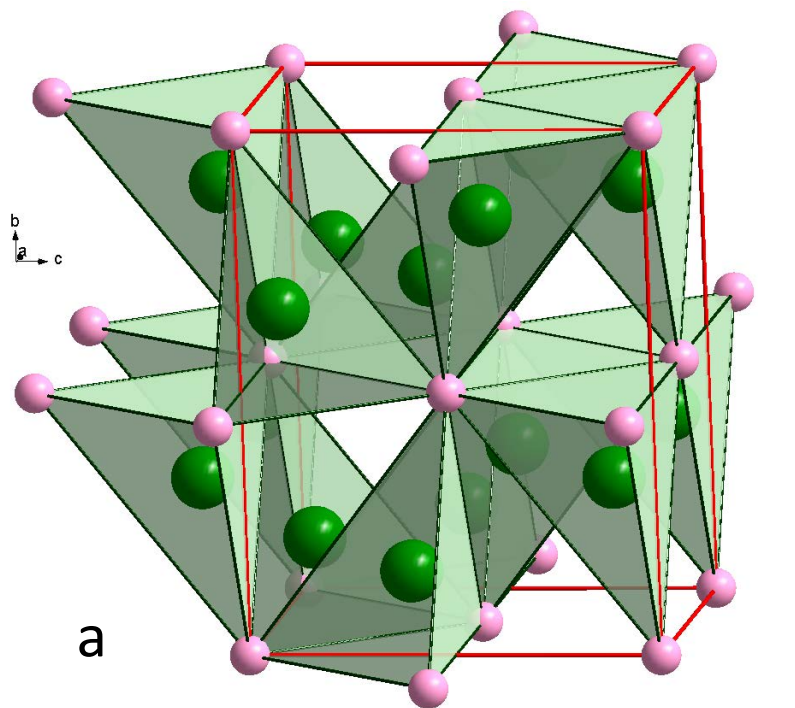
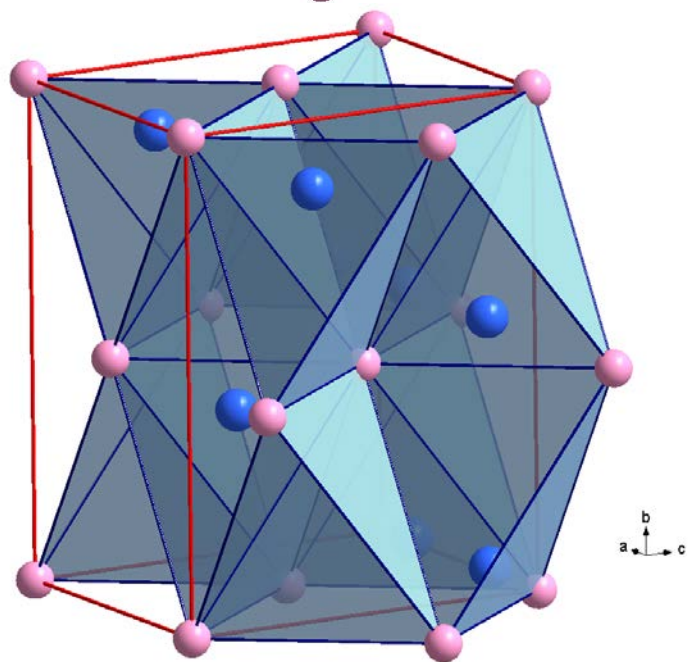


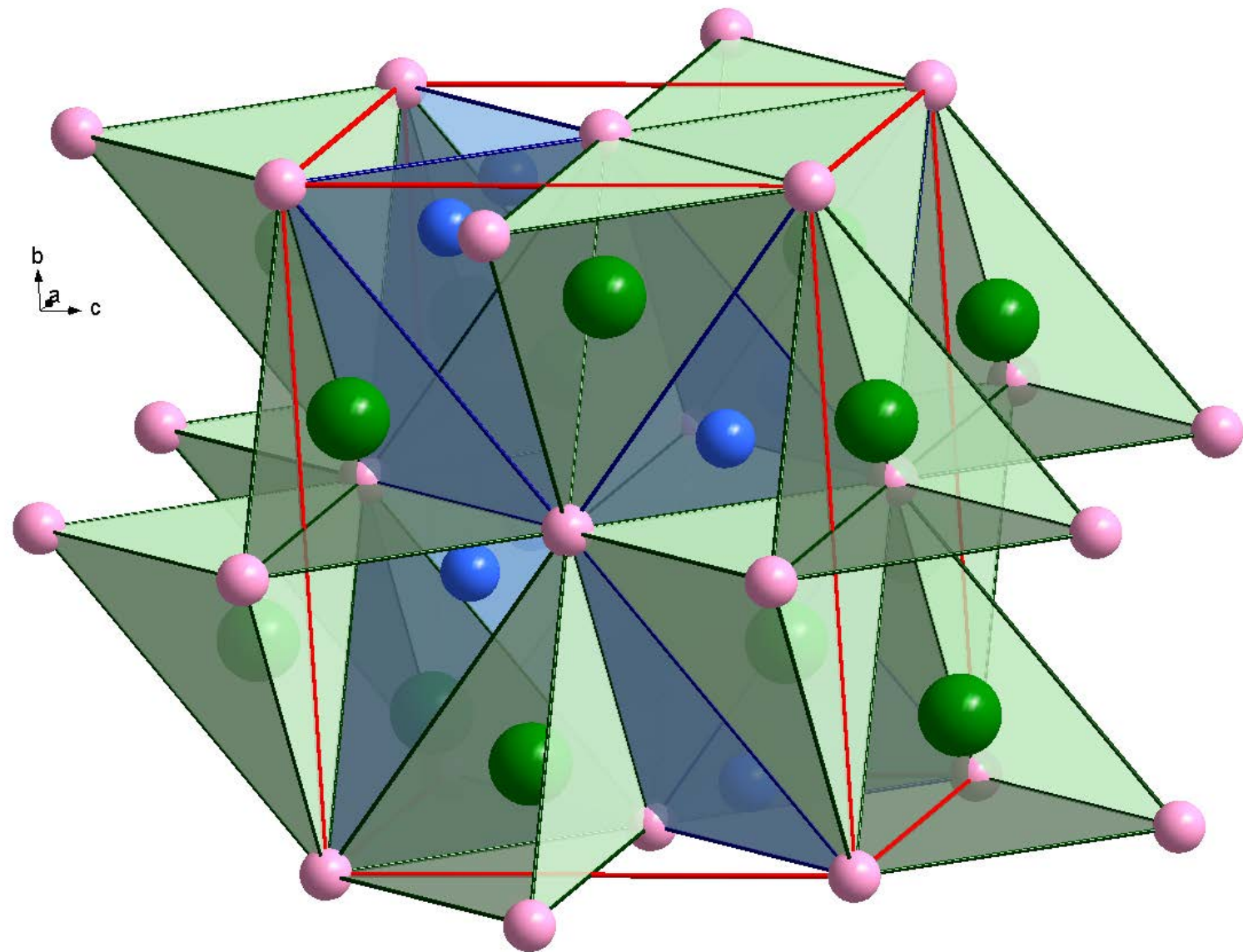
Figure 3



a

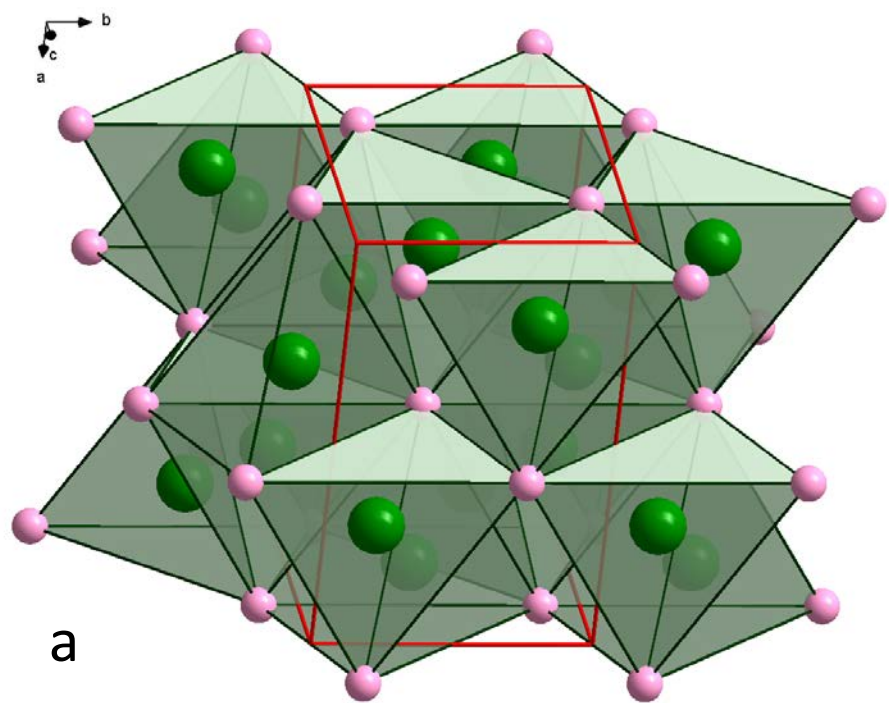


b

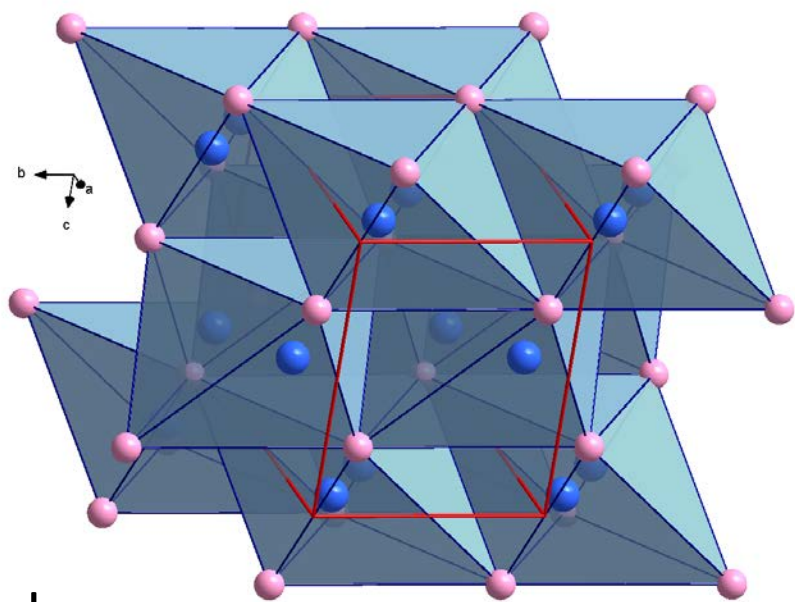


c

Figure 4



a



b

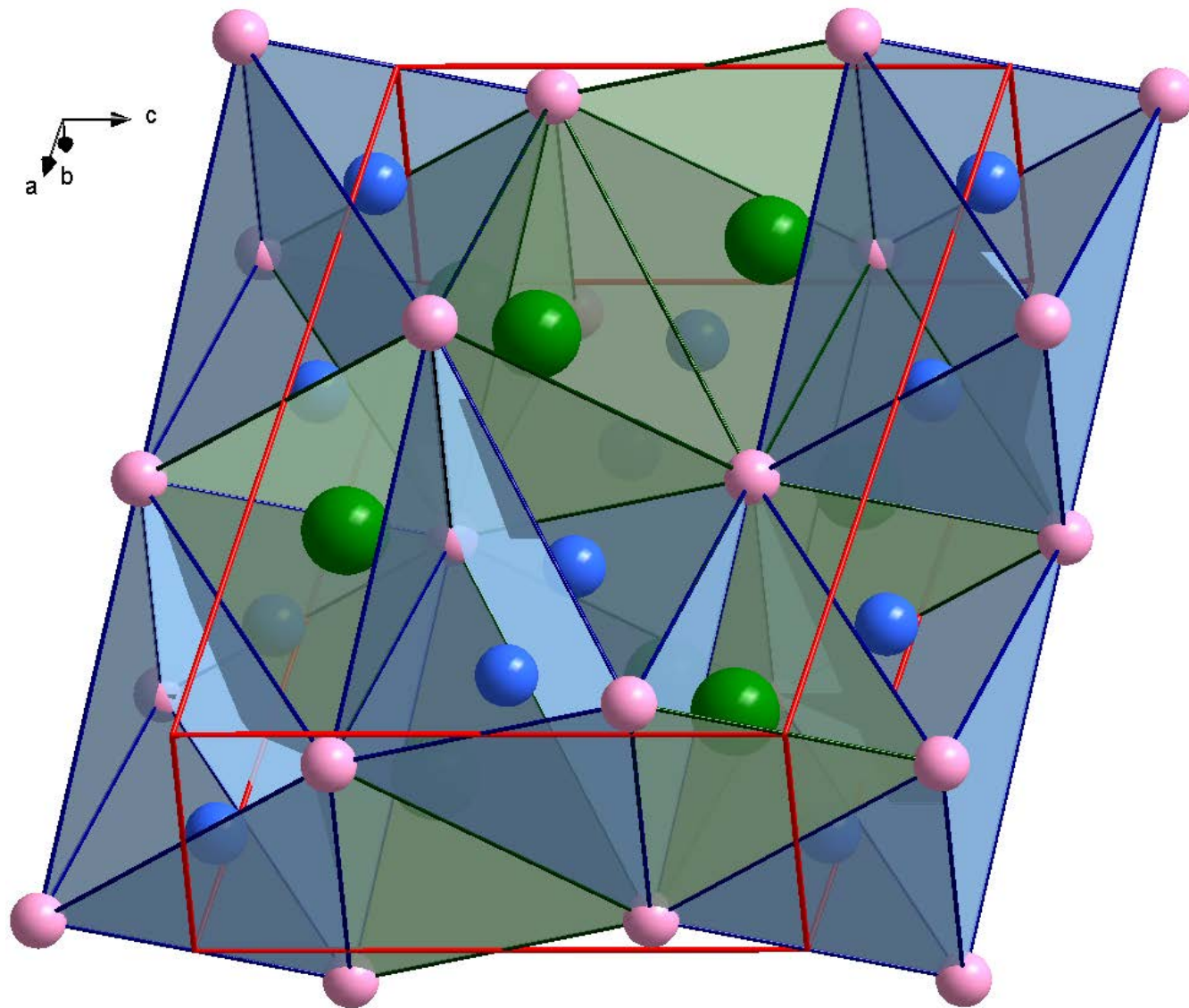


Figure 5

c

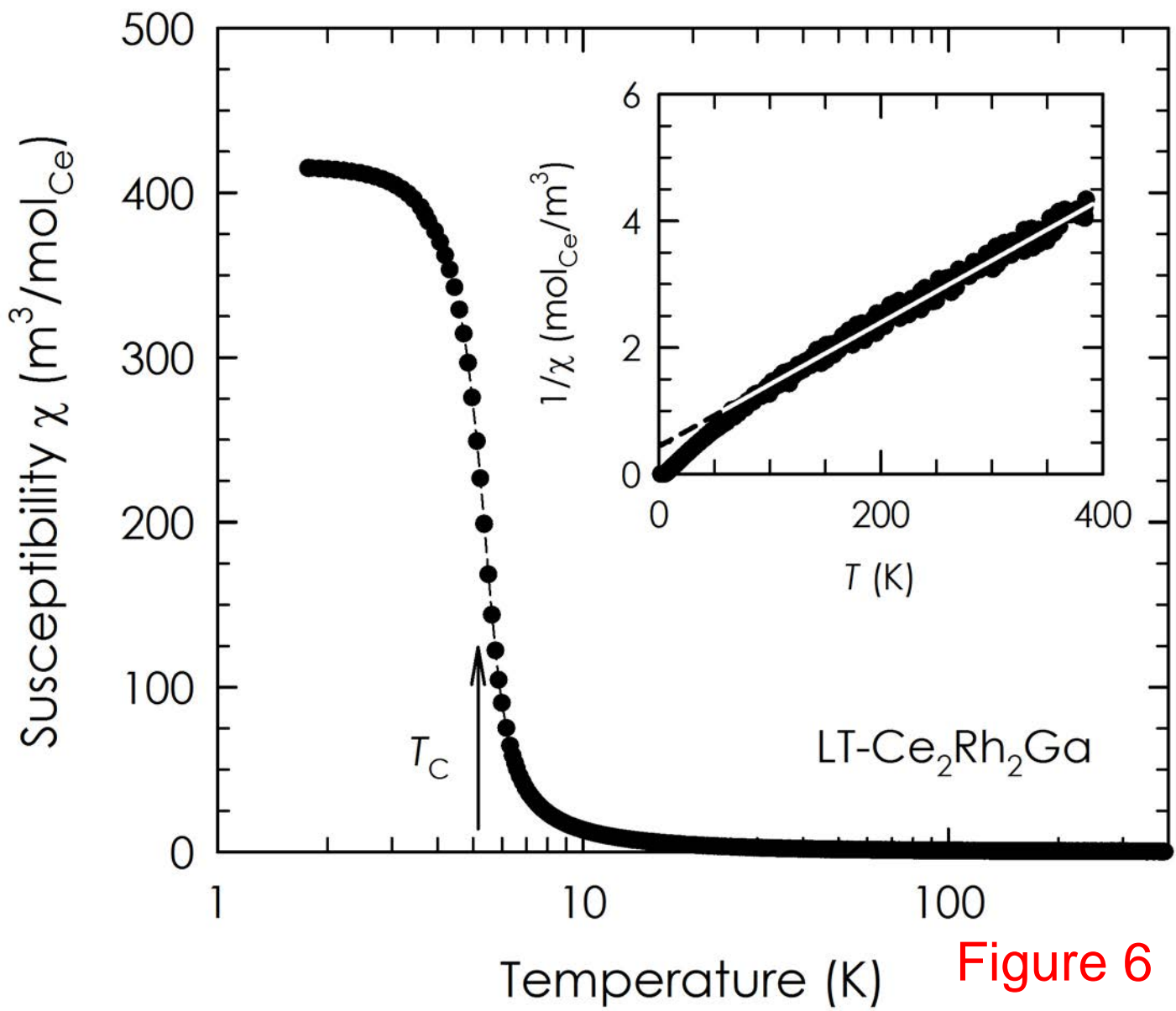


Figure 6

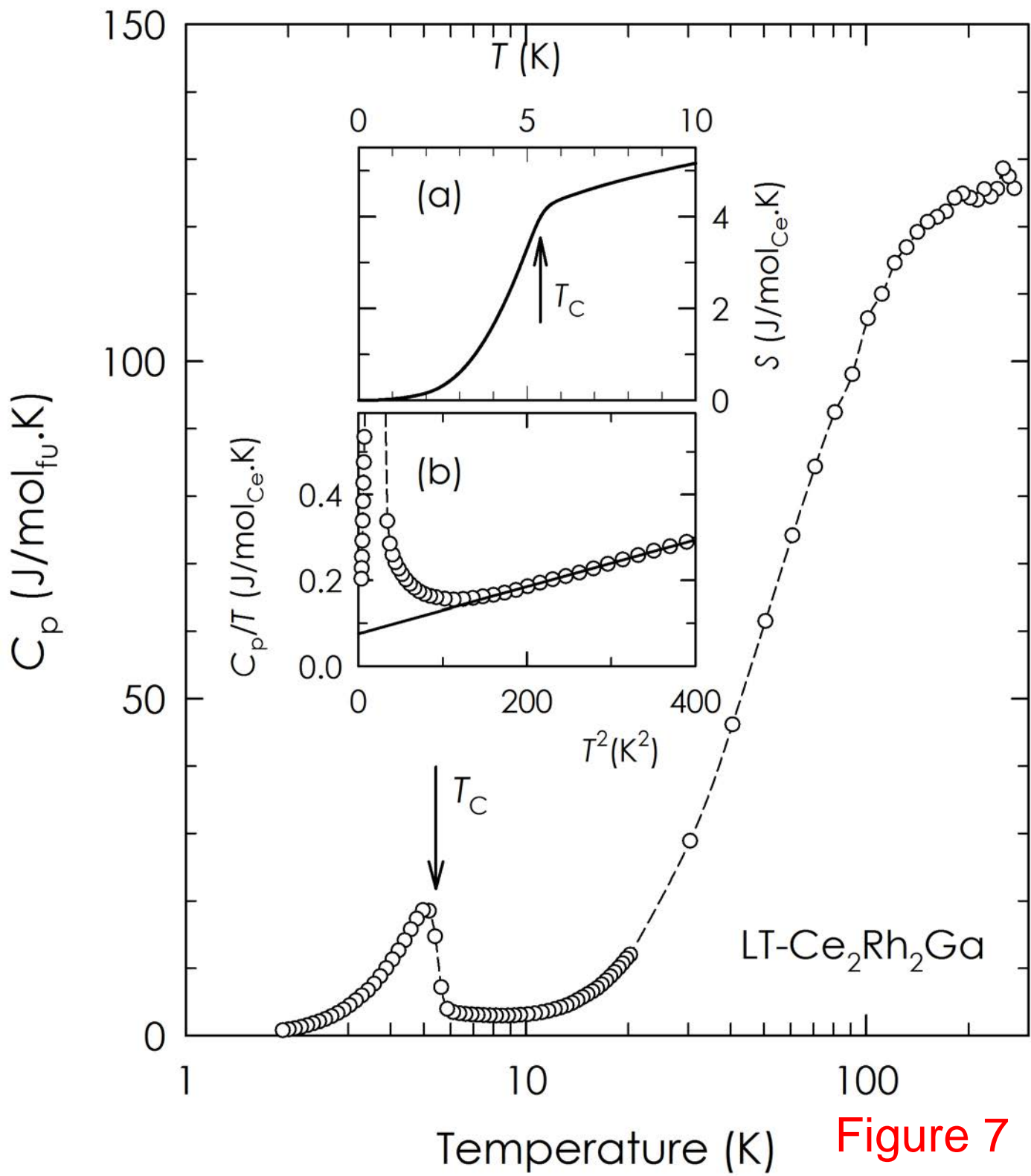
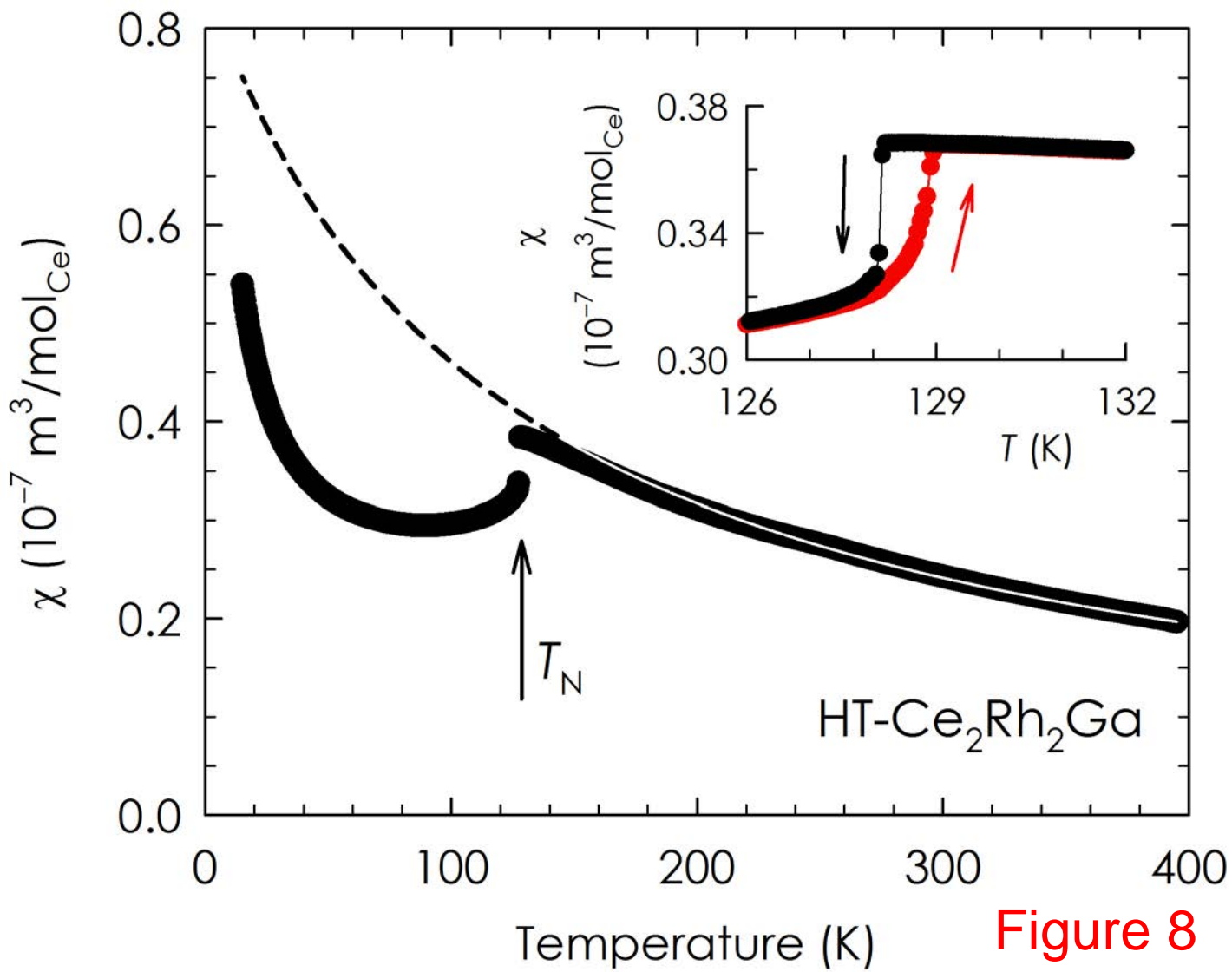


Figure 7



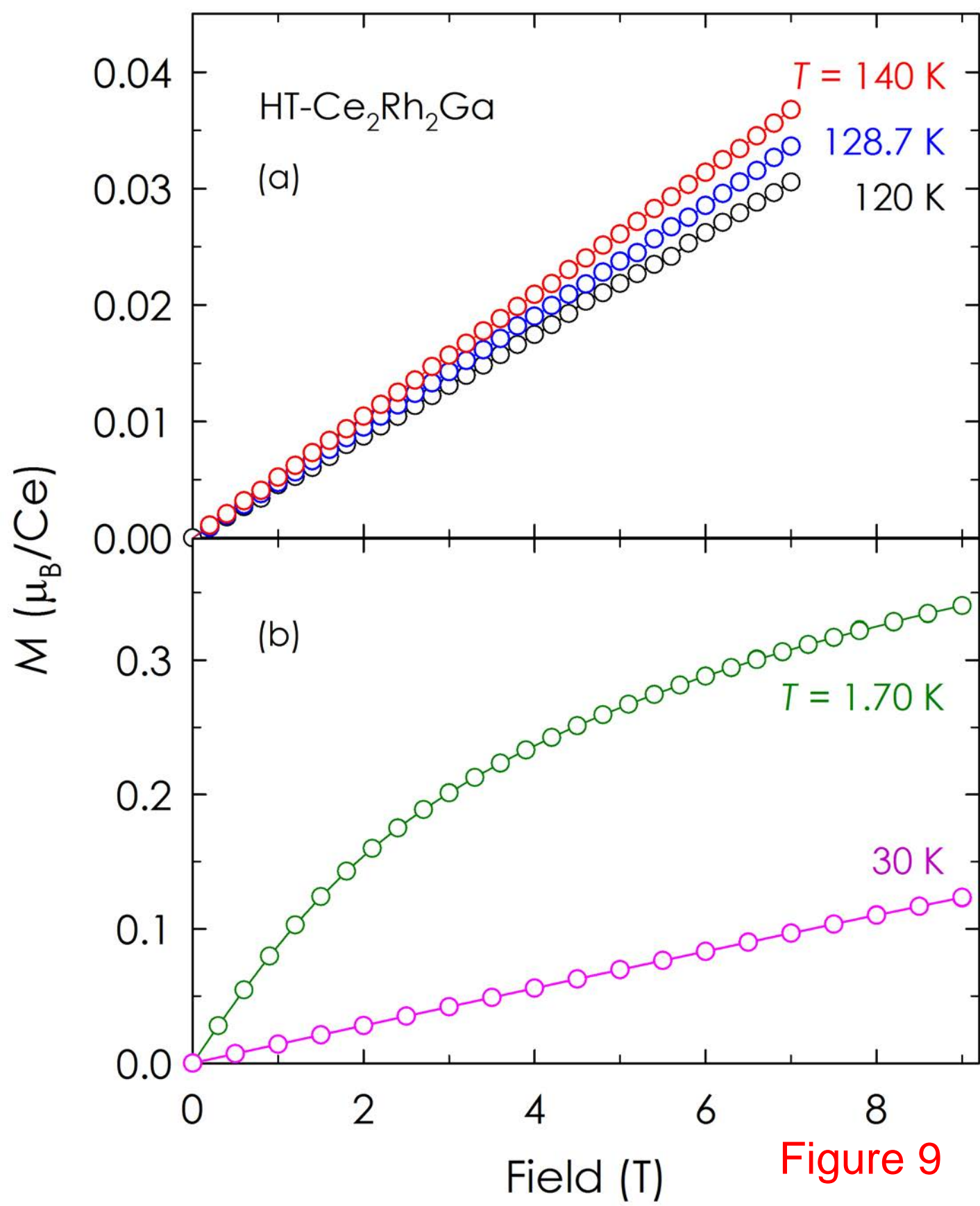


Figure 9

